Artificial Neural Network Encoding of Molecular Wavefunction for Quantum Computing

Masaya Hagai,*,† Mahito Sugiyama,‡ Koji Tsuda,¶,§,⊥ and Takeshi Yanai*,‖,†

†*Department of Chemistry, Nagoya University, Furocho, Chikusa Ward, Nagoya, Aichi 464-8601, Japan*
‡*National Institute of Informatics, 2-1-2 Hitotsubashi, Chiyoda-ku, Tokyo 101-8430, Japan*
¶*Graduate School of Frontier Sciences, The University of Tokyo, 5-1-5 Kashiwa-no-ha, Kashiwa, Chiba 277-8561, Japan*
§*RIKEN Center for Advanced Intelligence Project, 1-4-1 Nihonbashi, Chuo-ku, Tokyo 103-0027, Japan*
‖*Institute of Transformative Bio-Molecules (WPI-ITbM), Nagoya University, Furocho, Chikusa Ward, Nagoya, Aichi 464-8601, Japan*
⊥*Research and Services Division of Materials Data and Integrated System, National Institute for Materials Science, Ibaraki 305-0047, Japan*

E-mail: hagai.masaya.v9@s.mail.nagoya-u.ac.jp; yanait@chem.nagoya-u.ac.jp

Abstract

Artificial neural networks (ANNs) for material modeling have received significant interest. We recently reported an adaptation of ANNs based on Boltzmann machine (BM) architectures to an ansatz of the multiconfigurational many-electron wavefunction, designated neural-network quantum state (NQS), for quantum chemistry calculations. Here, this study presents its extended formalism to a quantum algorithm that enables the preparation of the NQS through quantum gates. The descriptors of the ANN model, which are chosen as occupancies of electronic configurations, are quantum-mechanically represented by qubits. Our algorithm may thus bring potential advantages over classical sampling-based computation employed in the previous studies. The NQS can be accurately formed through the quantum-native procedures, but the training of the model in terms of energy minimization is performed on a classical computer; thus, our approach is a class of variational quantum eigensolver. The BM models are related to the Gibbs distribution, and our preparation procedures exploit techniques of quantum phase estimation but with no Hamiltonian evolution. The proposed algorithm is assessed by implementing it on a quantum computer simulator. Illustrative molecular calculations at the complete-active-space configuration interaction level of theory are displayed, confirming consistency with the accuracy of our previous classical approaches.

1 Introduction

Machine learning (ML) with artificial neural networks (ANNs) has been recognized as a versatile and highly practicable approach to data analysis over recent periods.[1] Its marked abilities to compress and extract features from large-scale, high-dimensional data have considerable impacts on various fields. In computational chemistry, its highlighted applications encompass protein structure prediction,[2] improvement of density functionals,[3] molecular fingerprints,[4] accurate potential functions,[5] and many others.[6]

The use of ANN architectures as models of quantum many-particle physics is a subject of research that has been drawing great interest. Carleo *et al.* proposed an intriguing ML-based approach to use a class of ANN-based generative model, the restricted Boltzmann machine (RBM), for a representation of the quantum many-body state.[7–13] In this approach, the coefficients of the linear combination of many-body basis in the quantum superposition are parameterized with the RBM autoencoder in which a configuration vector of spins (↑ or ↓) or electron occupancies (0 or 1) serves as descriptors. This wavefunction ansatz is referred to as the neural-network quantum state (NQS). The scheme related to reinforcement learning is used to train the network parameters without prior knowledge or datasets, finding the best possible representation of the ground state as a solution of Schrödinger equation for the given Hamiltonian. Ref. 7 demonstrated high applicability towards physical systems with quantum Ising and Heisenberg models.

This inspiring but transparent formalism by Carleo and Troyer to use ML technology for a wavefunction solver has led various groups to its application to first-principles electronic structure calculations for chemical and material systems.[11,14–23] Xia and Kais reported the earliest study that used the RBM-based NQS for *ab initio* electronic structure calculations for molecules with an additional focus on its extension to a hybrid quantum-classical algorithm[14] along a similar line to this work. Our group previously presented an adaptation of the NQS as an encoder of the quantum chemical multireference wavefunction with complete-active-space configuration interaction (CAS-CI) model.[15] Our interest attaches to NQS's applicability as a solver to describe the so-called static electron (or multireference) correlation, whose quantum complexity often becomes challenging, particularly when studying multiple bond breaking, state-degeneracies, and varying radical nature in reactions, etc. The CAS-CI method is a basic framework of the approach to the static correlation problem based on the CI (or linear) expansion into electronic configuration basis spanning the chemically important part of the Hilbert space.[24,25]

In Ref. 15, we further proposed using the high-order Boltzmann machine (HBM), which is hidden-node free, in

place of the RBM from an alternative perspective – specifically, the second- and third-order BM models, termed BM2 and BM3, respectively. The earlier informatics studies of the HBM model[26,27] indicate that the BM3 can extract higher-order features to a comparable degree to RBM and, more importantly, yields the concave log-likelihood function where the RBM renders it nonconcave. The pilot implementation of the quantum-chemical NQS was achieved based on the BM2, BM3, and RBM architectures, demonstrating that the trained wavefunctions for illustrative molecules delivered desirable convergence to the CAS-CI results. We confirmed that the native combinatorial complexity arising from the evaluations of the energy, gradients, and partition function could be mitigated by stochastic sampling approaches in ML using the Markov chain Monte Carlo (MCMC) technique. However, this MCMC-based integration remains the most computationally demanding, practically hindering calculations with larger active space. A promising direction to address this issue may be, as typical to the prevalent ML computation, to carry out the MCMC process on general-purpose computing on graphics processing units (GPGPU), which is considered to be advantageous over traditional central processing units (CPUs).[16–19]

In this study, we attempt to explore an alternative game-changing strategy by reformulating the ML of the wavefunction with NQS as a quantum algorithm that can run on a quantum computer (QC). The QC has been considered a future device that should enable the exponential speedup for combinatorial computation. The use of quantum computing for ML has been attracting great attention in recent years, and quantum algorithms oriented to the general-purpose ML have been extensively studied, emerging as a subfield referred to as quantum machine learning (QML).[28–35] There are numerous earlier developments of QML that underlie this work. Wiebe *et al.* presented a quantum process named GEQS (Gradient Estimation via Quantum Sampling) allowing for the preparation of the state in which the weights of the superposition obey the Gibbs distribution, corresponding to the probability modeled by RBM, as a function of a configuration of visible and hidden units.[28] Its procedure is based on the quantum algorithm developed by Poulin and Wocjan[30] for preparing the Gibbs state of interacting quantum objects through quantum circuits with the use of Kitaev's quantum phase estimation (QPE).[36,37] The algorithm of Ref. 28 incorporates a technique of quantum amplitude amplification/estimation (QAA/QAE)[38] into the state preparation for reducing the number of samples at a quadratic rate.

The development of QC algorithms for electronic structure calculations of quantum chemical research has been a topic of intensive research in the recent past. As reviewed by Refs. 39–44, there are two major canonical frameworks of the algorithm for estimating the ground state energy on a QC. One is the pioneering approach using the iterative QPE scheme proposed by Aspuru-Guzik *et al.*[45] It is considered to be susceptible to quantum noise and ill-suited for the use of the near-term QCs or noisy intermediate-scale quantum (NISQ) devices. The second framework is the variational quantum eigensolver (VQE),[46] which is a hybrid quantum-classical approach amenable to the NISQ devices. Its state preparation is carried out on a QC and can be potentially built from low-depth circuits but at the cost of an increasing number of measurements. Various wave function ansatze for the state preparation have been developed and cannot be all cited, but the most extensively studied is the unitary coupled-cluster (UCC) framework[46] and many others.[47,48]

In this work, we present the development of an algorithm to build the trained ANN object on a QC as a materialized representation of the theoretical molecular many-electron wavefunction. It is classified as a VQE type. Unlike UCC[46] or others,[47] the NQS ansatz does not require the prerequisite of the reference wavefunction nor involves any wave operators represented with excitation operators. The quantum algorithm of NQS preparation based on the BM2, BM3, and RBM energy functions is explored here as a primal objective. As mentioned earlier, the RBM-based NQS method as the VQE algorithm was similarly investigated by Xia and Kais.[14] However, their algorithm does not form NQS on a QC in full form, but only prepares an intermediate quantum state, which is in turn sampled randomly by measures to evaluate the energy and gradients as expectation values using the sampled data in a classical manner. Similarly, the preparation (or reconstruction) of the RBM-based NQS for quantum computing was explored on hardware by Torlai *et al.*[49] from a somewhat different perspective while again restricting the measurements to a finite number of samples against their formal exponential requirement. Formulating a full-fledged quantum process (or oracle) to prepare NQS via quantum circuits should be valued for meaningfully bridging a gap between VQE and QML and is carried out in this study. Through the training of the NQS, as was done fully classically in Ref. 15, we aim to solve the equation to determine the ground-state molecular electronic structure and associated energy at the CAS-CI level of theory, a suited *ab initio* quantum chemistry model to handle chemical systems involving multireference electron correlation.

2 Results and Discussion

We here describe a hybrid quantum-classical approach to the machine learning (ML) based on the NQS machinery to determine the CAS-CI wavefunction. The procedure is divided into two major tasks: the quantum computing process of the state preparation and the classical computing process to update the learning parameters (Figure 1). In what follows, we begin by outlining the network architecture of NQS and its training scheme. Subsequently, the quantum algorithm to form the NQS on a QC is described. The application of our algorithm to molecular calculations using a simulator is shown for verifying the viability of the algorithm.

Training of Boltzmann Machine Based Neural Networks as Many-Electron Wavefunction

The basic formulation of the NQS ansatz and its ML is based on the method of the NQS solver developed in our previous work[15] oriented to the ML executed on classical computation. Carleo and Troyer first introduced the NQS method using the restricted Boltzmann machine (RBM) for the ANN that serves as a generative model to represent the ground state of many-body quantum systems.[7] In Ref. 15, the use of a higher-order Boltzmann machine (HBM)[26,27] in place of RBM was additionally proposed to offer another route to an NQS model that can be well trained despite the absence of hidden nodes in its perception architecture. We investigated the HBM based on the fully visible BM with bipartite graphs, referred to as the second-order BM or BM2, and its extended variant with the inclusion of tripartite graphs, designated the third-order BM or BM3.

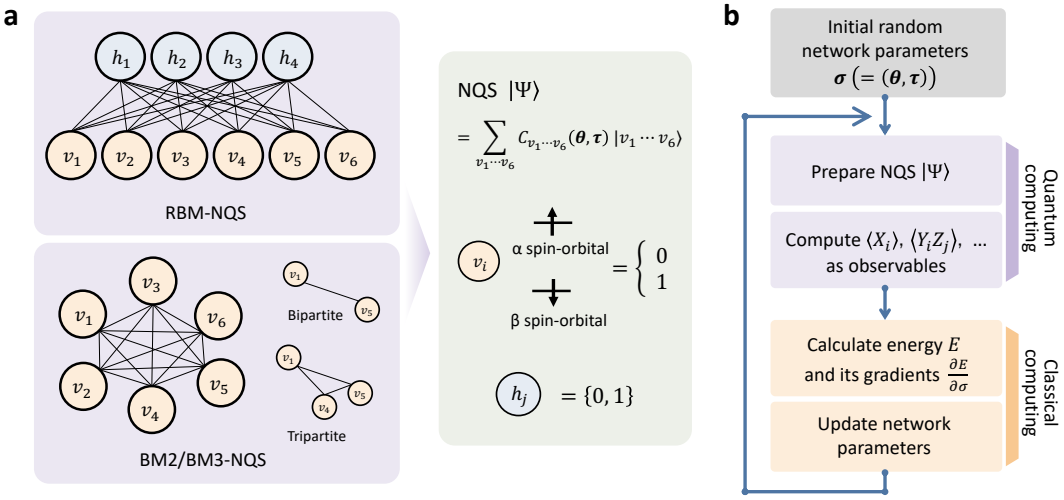

Figure 1: **a.** The neural networks architecture of NQS based on the RBM and HBM (BM2 and BM3) models. The binary signals of visible and hidden units are represented with qubits. **b.** Overall workflow of the hybrid quantum-classical algorithm to train the NQS model for the determination of the ground-state wavefunction and energy.

The probability distribution is modeled using the energy function, which is at the heart of the BM-based ANNs. It is given for BM2, BM3, and RBM as:

$$E^{\mathrm{BM2}}(\mathbf{v};\boldsymbol{\theta}) = \sum_{i}^{n_\mathrm{v}} v_i a_i + \sum_{ij}^{n_\mathrm{v}} v_i v_j w_{ij}\,, \tag{1}$$

$$E^{\mathrm{BM3}}(\mathbf{v};\boldsymbol{\theta}) = \sum_{i}^{n_\mathrm{v}} v_i a_i + \sum_{ij}^{n_\mathrm{v}} v_i v_j w_{ij} + \sum_{ijk}^{n_\mathrm{v}} v_i v_j v_k w_{ijk}\,, \tag{2}$$

$$E^{\mathrm{RBM}}(\mathbf{v},\mathbf{h};\boldsymbol{\theta}) = \sum_{i}^{n_\mathrm{v}} v_i a_i + \sum_{j}^{n_\mathrm{h}} h_j b_j + \sum_{ij}^{n_\mathrm{v},n_\mathrm{h}} v_i h_j w_{ij}\,, \tag{3}$$

respectively, where a_i and b_j are the biases associated with the visible nodes v_i and the hidden nodes h_j, respectively; and w_{ij} and w_{ijk} are the edge weights of the bipartite and tripartite interactions between the nodes, respectively. The joint parameters $\{a_i\} \oplus \{b_j\} \oplus \{w_{ij}\} \oplus \{w_{ijk}\}$ are denoted $\boldsymbol{\theta}$. The structures of the neural networks are sketched in Figure 1a.

Equations (1) to (3) are functions of bitstrings $\mathbf{v} \in \{0,1\}^{n_\mathrm{v}}$ and $\mathbf{h} \in \{0,1\}^{n_\mathrm{h}}$. In the present approach, the binary signal of the unit $v_i = 0, 1$ is seamlessly homologized to the two levels of a qubit; the same applies to the binary unit $h_j = 0, 1$. With this mapping between nodes and qubits, a superposition of $\{|\mathbf{v}\rangle\}$ in the NQS, written as

$$|\Psi\rangle = \sum_{\mathbf{v}} C_\mathbf{v} |\mathbf{v}\rangle\,, \tag{4}$$

can be formed on a QC, where the coefficients $C_\mathbf{v}$ are numerically determined by the training under the condition $\sum_\mathbf{v} |C_\mathbf{v}|^2 = 1$. We use this $|\Psi\rangle$ prepared on a QC as a central computational object that serves as a representation of the CAS-CI wavefunction of quantum chemistry calculation.

As a viable form of NQS for quantum computing, we use the following ansatz for structuring $C_\mathbf{v}$,[15]

$$C_\mathbf{v} = \underbrace{e^{\frac{\mathrm{i}}{2}E^{\mathrm{BM2}}(\mathbf{v};\boldsymbol{\tau})}}_{\text{phase}} \underbrace{\sqrt{\frac{1}{Z(\boldsymbol{\theta})} f(\mathbf{v};\boldsymbol{\theta})}}_{\text{amplitude}}\,, \tag{5}$$

where $Z(\boldsymbol{\theta})$ acts as the partition function $Z(\boldsymbol{\theta}) = \sum_\mathbf{v} f(\mathbf{v};\boldsymbol{\theta})$, and $f(\mathbf{v};\boldsymbol{\theta})$ has three variants defined by

$$f(\mathbf{v};\boldsymbol{\theta}) = \begin{cases} e^{E^{\mathrm{BM2/BM3}}(\mathbf{v};\boldsymbol{\theta})} & \text{(BM2/BM3)} \\ \left(\sum_\mathbf{h} \sqrt{e^{E^{\mathrm{RBM}}(\mathbf{v},\mathbf{h};\boldsymbol{\theta})}}\right)^2 & \text{(RBM)} \end{cases}\,, \tag{6}$$

for BM2, BM3, and RBM, respectively. Equation (5) is formulated using the two BMs associated with two different network parameter sets $\boldsymbol{\theta}$ and $\boldsymbol{\tau}$ (which are real-valued) to encode the amplitude and phase segments of $C_\mathbf{v}$, respectively. Note that for BM3 and RBM, the form of $C_\mathbf{v}$ (eq. (5)) somewhat differs from the definitions employed in Ref. 15. This ansatz indicates that by measuring $|\Psi\rangle$, it collapses onto a certain bit configuration $\mathbf{v}$ with the probablity $|C_\mathbf{v}|^2 = \frac{1}{Z(\boldsymbol{\theta})} f(\mathbf{v};\boldsymbol{\theta}) \equiv \mathcal{P}(\mathbf{v};\boldsymbol{\theta})$, which has no dependence on $\boldsymbol{\tau}$ (phase). Note that in eq. (5), the phase segment formulated and implemented in this work is limited to the BM2; however, we can readily formulate the preparation of the state that uses the BM3 and RBM models in its place.

Now let a joint set of the parameters be defined as $\boldsymbol{\sigma} \equiv (\boldsymbol{\theta}, \boldsymbol{\tau})$. The update of the whole parameters $\boldsymbol{\sigma}$ for the training of the BM models is a task that can be processed efficiently on classical computation. It is achieved in terms of finding a variationally optimal $\boldsymbol{\sigma}$ based on energy minimization. This optimization is related to reinforcement learning in the sense that neither reference data nor prior knowledge of the wavefunction is used. For the updating, we use the gradients of the energy E $(= \langle\Psi|H|\Psi\rangle)$ with respect to the parameters, which are calculated to be $\frac{\partial E}{\partial \sigma} = 2\,\mathrm{Re}\left[\langle HO^\sigma\rangle - \langle H\rangle\langle O^\sigma\rangle\right]$ where the Hamiltonian H is given from a user-specified chemical structure in the first-principles manner, and O^σ is written in the locally-discretized form with the basis $|\mathbf{v}\rangle$ as $O^\sigma_\mathbf{v} = \frac{\partial}{\partial \sigma} \log C_\mathbf{v}$ (see Ref. 15 for more details). Iteratively updating $\boldsymbol{\sigma}$ leads us to determine the optimal parameters

that meet the variational condition $\frac{\partial E}{\partial \sigma} = 0$ (Figure 1b).

As discussed in Section S1.6, the quantity $\langle H \rangle$ (= $\langle \Psi | H | \Psi \rangle$) is an object that can be evaluated as a sum of Pauli operator terms measured with Ψ prepared with the given neural network parameters $\boldsymbol{\sigma}$. Importantly, in the case of BM2, BM3, or other HBM, this simplicity can be further applied to $\langle HO^\sigma \rangle$ and $\langle O^\sigma \rangle$ for gradients (eqs. (S19)–(S20)); thus, the QC efficiency can fully benefit the computation of these quantities via quantum-native processes. However, for RBM, the gradient-related objects $\langle HO^\sigma \rangle$ and $\langle O^\sigma \rangle$ cannot be simply evaluated in a similar manner because of the presence of the sigmoid function (Sig) in its gradient formulas (eq. (S21)). With the QC simulator, we evaluate Sig in RBM's gradients in a classical manner. The state preparation will be discussed in detail later. In the previous implementations tailored to classical computing, these expectation values are evaluated using the stochastic approach. This is a widely-used ML technique, which takes a statistic average from Markov chain Monte Carlo (MCMC) sampling over the distribution generated by the ML model. This classical sampling process is fully replaced by the quantum computing procedure in this study.

Quantum Algorithm for Preparing Neural Network State

Here let us detail our proposed algorithm to construct the NQS representation of Ψ on a QC through quantum circuits. It is highly related to the quantum algorithms to sample the Gibbs distribution, such as GEQS[28] and others.[30] The overall procedures, consisting of several steps, are outlined in Figure 2, and its pseudo-program is displayed in Algorithm 1.

Qubits architecture: Qubits used in the present algorithm are classified into four groups: visible, hidden, ancilla, and energy register (Figure 2a). Let n_v and n_h refer to the numbers of the visible and hidden qubits, respectively, which are equal to those of the visible and hidden nodes of the BM models (eqs. (1) to (3)), respectively. We use an equal number of qubits for the ancilla and energy register; thus, it is commonly denoted n_reg. The numeric precision of a single value stored in the energy register is determined by n_reg, which is user-specified and bears a relation with the permitted error ϵ as $n_\mathrm{reg} = \log_2(1/\epsilon)$.

QPE based procedure: The state preparation begins by initializing the state $|\Psi\rangle$ in $|0\rangle$, as denoted in the following expression: $|\Psi\rangle \to |0\rangle$. In the rest of this section, unless otherwise noted, we focus solely on the BM2 model for simplicity, which has no hidden nodes. The theory and formalisms for BM2 can be readily applied to the BM3 model as well as the RBM model that has hidden nodes, although tangible procedures will not be shown.

Then, we apply the Hadamard gate on all the visible qubits, forming the following uniform superposition in the visible qubit space:

$$|\Psi\rangle \to \frac{1}{\sqrt{2^{n_\mathrm{v}}}} \sum_{\mathbf{v}} |\mathbf{v}\rangle |\mathbf{0}\rangle_{n_\mathrm{reg}} |\mathbf{0}\rangle_{n_\mathrm{reg}} \ . \tag{7}$$

As an alternative to this state, we may employ a uniform superposition of the subgroup of $\{|\mathbf{v}\rangle\}$ built under the constraint of the particle-number (PN) symmetry[51] (see also Section 4 for details); indeed, this is extensively used in our test calculations. The PN-conserving preparation circuit for the case of the singlet state with four electrons in four orbitals is shown in Supporting Information.

Algorithm 1 Algorithm to prepare quantum state representing NQS with BM2 model [a]

Input: Model parameters $\boldsymbol{\theta}$ and $\boldsymbol{\tau}$.
Output: Quantum state $|\Psi\rangle$ representing NQS
procedure
  Initialize $|\Psi\rangle$ in $|\mathbf{0}\rangle_{n_\mathrm{v}} |\mathbf{0}\rangle_{n_\mathrm{reg}} |\mathbf{0}\rangle_{n_\mathrm{reg}}$.
  Apply the Hadamard gate on all visible qubits:
    $|\Psi\rangle \to \frac{1}{\sqrt{2^{n_\mathrm{v}}}} \sum_{\mathbf{v}} |\mathbf{v}\rangle |\mathbf{0}\rangle_{n_\mathrm{reg}} |\mathbf{0}\rangle_{n_\mathrm{reg}}$ ▷ eq. (7)
  Determine max and min $E^{\mathrm{BM2}}(\mathbf{v};\boldsymbol{\theta})$.
    ▷ E.g., quantum annealing learning search [50]
  Find D and Δ such that $\tilde{E}_{\mathbf{v}}(\boldsymbol{\theta}) \forall \mathbf{v} \in \{0,1\}^{n_\mathrm{v}}$ ranges from 0 to 1
    where $\tilde{E}_{\mathbf{v}}(\boldsymbol{\theta}) \equiv E^{\mathrm{BM2}}(\mathbf{v};\boldsymbol{\theta})/D + \Delta$.
  Perform the QPE procedure (Algorithm S1):
    $|\Psi\rangle \to \frac{1}{\sqrt{2^{n_\mathrm{v}}}} \sum_{\mathbf{v}} |\mathbf{v}\rangle \left|\tilde{\mathbf{E}}_{\mathbf{v}}\right\rangle_{n_\mathrm{reg}} |\mathbf{0}\rangle_{n_\mathrm{reg}}$ ▷ eq. (8)
    using the energy curation gate $U = e^{2\pi \mathrm{i}\, \tilde{E}_{\mathbf{v}}(\boldsymbol{\theta})}$ (Algorithm S2).
  for $k = 1 \ldots n_\mathrm{reg}$ **do**
    Apply the $R_y(\Theta)$ gate on k-th ancilla qubit
      with the angle $\Theta = 2 \arccos\left(e^{-D\, 2^{-(k+1)}}\right)$
      conditioned on k-th energy register qubit $|0\rangle$.
  end for
    $|\Psi\rangle \to C' \left\{ \sum_{\mathbf{v}} \sqrt{\frac{e^{E^{\mathrm{BM2}}(\mathbf{v};\boldsymbol{\theta})}}{Z}} |\mathbf{v}\rangle \left|\tilde{\mathbf{E}}_{\mathbf{v}}\right\rangle_{n_\mathrm{reg}} |\mathbf{0}\rangle_{n_\mathrm{reg}} + \cdots \right\}$
    ▷ eq. (12)
    C' serves as normalization, automatically accounting
    for a factor asscoiated with $\sqrt{\frac{e^{D\Delta}}{Z}}$.
  Perform the reverse QPE procedure (Algorithm S1):
    $|\Psi\rangle \to C'' \left\{ \sum_{\mathbf{v}} \sqrt{\frac{e^{E^{\mathrm{BM2}}(\mathbf{v};\boldsymbol{\theta})}}{Z}} |\mathbf{v}\rangle |\mathbf{0}\rangle_{n_\mathrm{reg}} |\mathbf{0}\rangle_{n_\mathrm{reg}} + \cdots \right\}$
    ▷ eq. (13)
    with $U = e^{2\pi \mathrm{i}\, \tilde{E}_{\mathbf{v}}(\boldsymbol{\theta})}$ (Algorithm S2).
  Apply QAA procedure (Algorithm S4) on $|\Psi\rangle$
    to ancilla qubits $|\mathbf{0}\rangle_{n_\mathrm{reg}}$.
  Observe ancilla qubits.
  if the anicilla qubits $\neq |\mathbf{0}\rangle_{n_\mathrm{reg}}$ **then**
    Start over from the begining.
  end if
  Now, $|\Psi\rangle \to \sum_{\mathbf{v}} \sqrt{\frac{e^{E^{\mathrm{BM2}}(\mathbf{v};\boldsymbol{\theta})}}{Z}} |\mathbf{v}\rangle |\mathbf{0}\rangle_{n_\mathrm{reg}} |\mathbf{0}\rangle_{n_\mathrm{reg}}$ ▷ eq. (14)
  Perform the phase preparation procedure (Algorithm S3).
    $|\Psi\rangle \to \sum_{\mathbf{v}} e^{\frac{\mathrm{i}}{2} E^{\mathrm{BM2}}(\mathbf{v};\boldsymbol{\tau})} \sqrt{\frac{e^{E^{\mathrm{BM2}}(\mathbf{v};\boldsymbol{\theta})}}{Z}} |\mathbf{v}\rangle |\mathbf{0}\rangle_{n_\mathrm{reg}} |\mathbf{0}\rangle_{n_\mathrm{reg}}$
    ▷ eq. (15)
  return $|\Psi\rangle$
end procedure

[a] The procedure can readily be applied to BM3 and RBM models with a minor change.

The next step is to obtain the following state by transforming eq. (7) via Kitaev's QPE procedure:[36]

$$|\Psi\rangle \to \frac{1}{\sqrt{2^{n_\mathrm{v}}}} \sum_{\mathbf{v}} |\mathbf{v}\rangle \left|\tilde{\mathbf{E}}_{\mathbf{v}}\right\rangle_{n_\mathrm{reg}} |\mathbf{0}\rangle_{n_\mathrm{reg}} \ , \tag{8}$$

where $\tilde{\mathbf{E}}_{\mathbf{v}}$ is a binary representation of the converted energy of E (eqs. (1) to (3)) as a function the configuration $\mathbf{v}$ is stored in the energy register qubits. The binary number $\tilde{\mathbf{E}}_{\mathbf{v}} =: \tilde{E}^1_{\mathbf{v}} \tilde{E}^2_{\mathbf{v}} \ldots \tilde{E}^{n_\mathrm{reg}}_{\mathbf{v}}$ ($\tilde{E}^i_{\mathbf{v}} = 0, 1$) encodes the decimal number $\tilde{E}^1_{\mathbf{v}} 2^{-1} + \tilde{E}^2_{\mathbf{v}} 2^{-2} + \ldots + \tilde{E}^{n_\mathrm{reg}}_{\mathbf{v}} 2^{-n_\mathrm{reg}}$, expressing $\tilde{E}_{\mathbf{v}}$ in a finite precision. The converted energy $\tilde{E}_{\mathbf{v}}$ is a mapping of the energy function $E(\mathbf{v};\boldsymbol{\theta})$ (eqs. (1) to (3)) into a value ranging from 0 to 1. In this study, it is parameterized as

$$\tilde{E}_{\mathbf{v}}(\boldsymbol{\theta}) \equiv E(\mathbf{v};\boldsymbol{\theta})/D + \Delta \tag{9}$$

with the scaling constant D and shifting constant Δ. By preparing $E^{\max} = \max_{\mathbf{v}} E(\mathbf{v};\boldsymbol{\theta})$ and $E^{\min} = \min_{\mathbf{v}} E(\mathbf{v};\boldsymbol{\theta})$, the constants D and Δ can be given as $D = (E^{\max} - E^{\min})$ and $\Delta = -E^{\min}/D$, ensuring that $\left|\tilde{\mathbf{E}}_{\mathbf{v}}(\boldsymbol{\theta})\right\rangle$ varies between $|00\ldots0\rangle_{n_\mathrm{reg}}$ and $|11\ldots1\rangle_{n_\mathrm{reg}}$. Finding $E^{\max}$ and $E^{\min}$ are

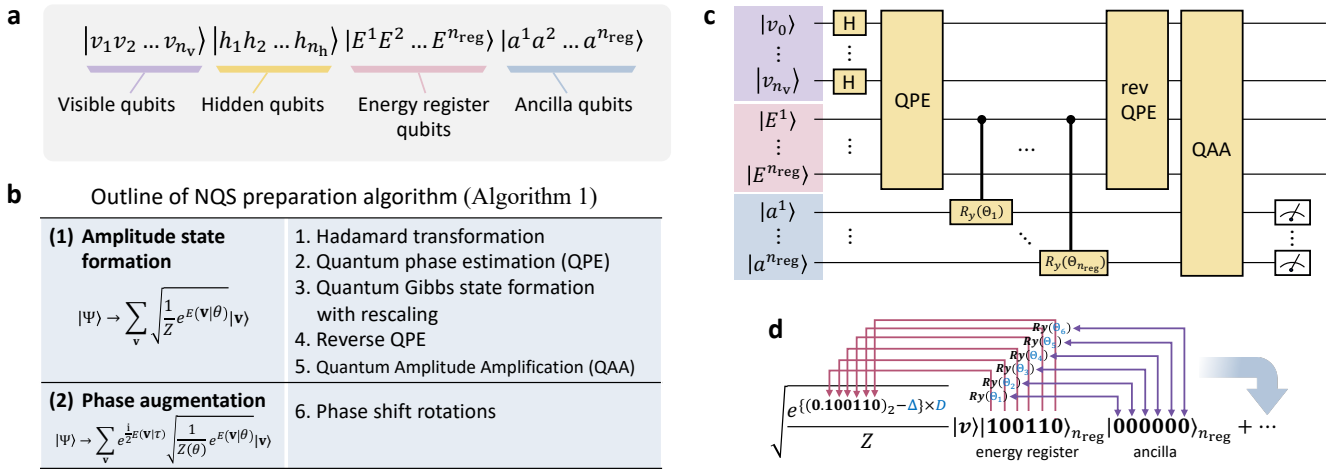

Figure 2: **a.** Qubit architecture employed in this study. **b.** The whole procedural steps of the state preparation of the NQS on a QC. **c.** Graphical representation of quantum circuit to prepare the Gibbs state (eq. (14)). **d.** Illustrative process of the bitwise operations to evaluate the Gibbs factor using the controlled R_y gate.

subject to the QUBO problem and possibly obtained via quantum annealing.[50] We will not investigate the quantum computing of $E^{\max}$ and $E^{\min}$ in detail, which is assumed to be carried out using the third-party quantum algorithms as a subprocess of our algorithm.

The QPE algorithm is a technique to find θ_n of the eigenvalue $e^{2\pi \mathrm{i}\,\theta_n}$ on a QC, given the unitary operator U and eigenvector $|\psi_n\rangle$ such that $U|\psi_n\rangle = e^{2\pi \mathrm{i}\,\theta_n}|\psi_n\rangle$.[36] The QPE based procedure is shown in Algorithm S1 with its subroutine for U Algorithm S2. The structure of U is a key ingredient to realize the formation of eq. (8) via the QPE, and its quantum circuit, here named *energy curation* gate, should be built, in this case, based on the postulation $U|\mathbf{v}\rangle = e^{2\pi \mathrm{i}\,\tilde{E}_{\mathbf{v}}}|\mathbf{v}\rangle$. This U appears to behave as an evolution operator that attaches the converted BM energy function $\tilde{E}_{\mathbf{v}}$ via the phase kickback to the basis $|\mathbf{v}\rangle$ in $|\Psi\rangle$ non-iteratively. We underscore that it does not involve Hamiltonian evolution or Trotter steps. The quantum algorithm of applying U based on the phase shift rotation $R'_z(\theta)$ defined as,

$$R'_z(\theta) = \begin{pmatrix} 1 & 0 \\ 0 & e^{i\theta} \end{pmatrix} \tag{10}$$

with its controled gate is detailed in Algorithm S2. This quantum gate serves as a subroutine built into the QPE process (eq. (8)), as shown in Algorithm 1.

Quantum Gibbs state formation with rescaling: Let us proceed to the building of the Gibbs state from eq. (8) (Algorithm 1). A major part of this task aims to read out the stored $\tilde{E}_{\mathbf{v}}$ and transform it to the rescaled coefficient $\sqrt{\exp\{(\tilde{E}_{\mathbf{v}}(\boldsymbol{\theta}) - \Delta)/D\}}$ $(= \sqrt{e^{E(\mathbf{v};\boldsymbol{\theta})}})$, by which the basis of the superposition is scalarly scaled via the qubit rotations. In this operation, which is bitwise, the $R_y(\Theta)$ gate is applied on the k-th anicilla qubit with the angle $\Theta = 2\arccos\left(e^{-D\,2^{-(k+1)}}\right)$ conditioned on the k-th energy register qubit. This allows the state with the k-th ancilla qubit in the state $|0\rangle$ to be transformed as follows:

$$\begin{aligned} &\frac{1}{\sqrt{2^{n_{\mathrm{v}}}}}\sum_{\mathbf{v}}|\mathbf{v}\rangle\left|\tilde{\mathbf{E}}_{\mathbf{v}}\right\rangle_{n_{\mathrm{reg}}}|0\cdots 0^k\cdots 0\rangle_{n_{\mathrm{reg}}} \\ &\to \frac{1}{\sqrt{2^{n_{\mathrm{v}}}}}\sum_{\mathbf{v}}\sqrt{e^{(\tilde{E}^k_{\mathbf{v}}\,2^{-k})D}}\,|\mathbf{v}\rangle\left|\tilde{\mathbf{E}}_{\mathbf{v}}\right\rangle_{n_{\mathrm{reg}}}|0\cdots 0^k\cdots 0\rangle_{n_{\mathrm{reg}}} \\ &\quad + \frac{1}{\sqrt{2^{n_{\mathrm{v}}}}}\sum_{\mathbf{v}}\sqrt{1-e^{(\tilde{E}^k_{\mathbf{v}}\,2^{-k})D}}\,|\mathbf{v}\rangle\left|\tilde{\mathbf{E}}_{\mathbf{v}}\right\rangle_{n_{\mathrm{reg}}}|0\cdots 1^k\cdots 0\rangle_{n_{\mathrm{reg}}} \end{aligned} \tag{11}$$

By subsequently applying this transformation for $k = 1$ to n_{reg}, we achieve the key process to build the BM distribtuion of the amplitude segment of our NQS model $C_{\mathbf{v}}$ (eq. (5)) as follows:

$$\begin{aligned} |\Psi\rangle &\to C\left\{\sum_{\mathbf{v}}\sqrt{\exp\{(\tilde{E}^1_{\mathbf{v}}\,2^{-1} + \tilde{E}^2_{\mathbf{v}}\,2^{-2} + \cdots + \tilde{E}^{n_{\mathrm{reg}}}_{\mathbf{v}}\,2^{-n_{\mathrm{reg}}} - \Delta)D\}}\right. \\ &\qquad \left. \times\ |\mathbf{v}\rangle\left|\tilde{\mathbf{E}}_{\mathbf{v}}\right\rangle_{n_{\mathrm{reg}}}|\mathbf{0}\rangle_{n_{\mathrm{reg}}} + \cdots\right\} \\ &= C'\left\{\sum_{\mathbf{v}}\sqrt{\frac{e^{E(\mathbf{v};\boldsymbol{\theta})}}{Z}}\,|\mathbf{v}\rangle\left|\tilde{\mathbf{E}}_{\mathbf{v}}\right\rangle_{n_{\mathrm{reg}}}|\mathbf{0}\rangle_{n_{\mathrm{reg}}} + \cdots\right\}. \end{aligned} \tag{12}$$

The constants C and C' are adjustably settled due to the normalization nature of the state, and the partition function Z is fictitiously given at this moment but naturally establishes at the end. Note that the constant $\sqrt{e^{-D\Delta}}$ comes with the normalization C. It is important to note that the reconstructed $E(\mathbf{v};\boldsymbol{\theta})$ appearing in eq. (12) has a finite numeric precision in value, whose precision hinges on n_{reg}.

As written in Algorithm 1, we then apply the aforementioned QPE procedure (Algorithm S1) on Equation (12) in reverse, allowing the energy register qubits to revert to $|\mathbf{0}\rangle$ as follows:[28]

$$|\Psi\rangle \to C''\left\{\sum_{\mathbf{v}}\sqrt{\frac{e^{E(\mathbf{v};\boldsymbol{\theta})}}{Z}}\,|\mathbf{v}\rangle|\mathbf{0}\rangle_{n_{\mathrm{reg}}}|\mathbf{0}\rangle_{n_{\mathrm{reg}}} + \cdots\right\} \tag{13}$$

Next, a measurement is performed on the ancilla qubits. If $|\mathbf{0}\rangle_{n_{\mathrm{reg}}}$ is observed, the state is indicated to result in the formation of the Gibbs state:

$$|\Psi\rangle \to \sum_{\mathbf{v}}\sqrt{\frac{e^{E(\mathbf{v};\boldsymbol{\theta})}}{Z}}\,|\mathbf{v}\rangle\,, \tag{14}$$

where $1/\sqrt{Z}$ serves as the normalization constant. This observation occurs at a certain probability. Otherwise, the state preparation needs to be done from the beginning over again.

Finally, we turn to the preparation of the phase segment of eq. (5) as the rest of the task. We apply the phase shift roatation R'_z (section 2) on eq. (14) over all the visible qubits and furthermore apply its controlled gate over all the pairs (see also Algorithm S3 for details), finally obtaining the target NQS state:

$$|\Psi\rangle \rightarrow \sum_{\mathbf{v}} e^{\frac{\mathrm{i}}{2}E^{\mathrm{BM2}}(\mathbf{v};\boldsymbol{\tau})}\sqrt{\frac{e^{E(\mathbf{v};\boldsymbol{\theta})}}{Z}}\,|\mathbf{v}\rangle \tag{15}$$

It is used to compute energy as well as gradients required for training the model, and other observables such as reduced density matrices (RDMs), etc.

Use of Quantum Amplitude Amplification (QAA): As discussed earlier, we may fail to observe $|\mathbf{0}\rangle_{n_{\mathrm{reg}}}$ at a certain probability in the measurement on the ancilla qubits. This means that the whole identical steps to prepare the state eq. (14) from the initial state need to be reiterated until $|\mathbf{0}\rangle_{n_{\mathrm{reg}}}$ is successfully observed. In practice, an additional algorithm, referred to as the quantum amplitude amplification (QAA),[38] to increase the success rate is incorporated into the state preparation procedure, as shown in Algorithm 1. The QAA is related to Grover's algorithm and enables quadratically increasing the probability of finding the desired state. In Algorithm S4, the workflow of the QAA is shown in detail.

The QAA process carries out amplification iteratively. Given that the whole process of the state preparation to form eq. (14) is written as $|\Psi\rangle = S\,|0\rangle$, the whole process of the same S is repeatedly performs during the single QAA process. The important consequence is thus that the number of amplification iterations is thus a factor arising in the scaling of the circuit depth.

H_2 Potential Energy Curve Calculation

Let us now turn to numerical assessments of our approach using its prototype implementation on a QC simulator, for which we used the library QULACS.[52] As the first test case, the results here are presented on the bond dissociation energy curve of the H_2 molecule. Figure 3a shows the curves of the total energies determined by BM2(FS) and BM3(FS) with CMO and LMO basis and $n_{\mathrm{reg}} = 8$. For comparison, the RHF and full CI energies are also shown in the graph. The plots of the energies obtained with our approaches at all the points appear to match the full CI energies in good agreement. The correlation energy, corresponding to the difference in total energy between full CI and RHF, is increasingly larger with increasing bond length, exhibiting the degree of static or multireference correlation. Even at the structures with a large amount of electron correlation, the BM2 and BM3 models with 8-qubit energy registers were shown to yield accuracy consistent with the predictions at the near-equilibrium structures involving a small amount of electron correlation.

Figure 3b to 3e show the errors of the potential energy curves (PECs) relative to the full CI predictions as a function of tested n_{reg} for BM2/CMO, BM2/LMO, BM3/CMO, and BM3/LMO, respectively, prepared with the FS treatment. Regardless of the model and orbital type, the total energies with $n_{\mathrm{reg}} \geq 10$ are accurate to 10^{-6} $\mathrm{E_h}$, far exceeding the chemical accuracy (≈ 1 $m\mathrm{E_h}$). Roundoff errors associated with the truncation of energy register qubits were not wholly vanishing in the obtained energies even with $n_{\mathrm{reg}} = 10$ and 12, compared to the results with $n_{\mathrm{reg}} = 50$; however, they are negligible. The roundoff errors are systematically eliminated with increasing n_{reg}, exhibiting an approximately quadratic convergence with respect to n_{reg}. Interestingly, the coarsest representation of the energy registers with $n_{\mathrm{reg}} = 6$ corresponding to a precision of $2^{-6} \approx 0.016$ can produce errors in energy falling below 1 $m\mathrm{E_h}$. Overall, the energies were predicted better with LMOs than with CMOs for the given number of the energy register qubits. The BM3 does not consistently outperform the BM2 across the curves in this system. This conflicts the theoretical assumption but seems to be ascribed to the exceeding complexity of the BM3 parameterization against a rather simple structure of the H_2 wavefunction.

In Figure 3f to 3i, the errors of the PECs obtained with the models prepared as a PN state[51] with BM2/CMO, BM2/LMO, BM3/CMO, and BM3/LMO, respectively, are monitored. As detailed in Methods section, this preparation can efficiently train the BM models with a focus on the descriptors (i.e., configurations) conserving the target electron number. In this test system, the PN-conserving configurations amount to $6 = ({}_4C_2)$, which is much smaller than the dimension of FS, $16 = (2^4)$. This reduction should have a favored impact on the representability of the BM models. It was indeed confirmed in the drastic rectification of the errors observed in all the predicted PECs compared to those of the FS variants (Figure 3b to 3e).

The training as an FS state requires that the models predict the coefficients $C_{\mathbf{v}}$ to be exactly zero for the PN-unconserving $\mathbf{v}$. This particular requirement is imposed during the training process, i.e., optimizing $\boldsymbol{\theta}$ and $\boldsymbol{\tau}$; nonetheless, the optimization does not discriminate between the PN-conserving and -unconserving $\mathbf{v}$. In our experience with the FS-based calculations, the cost of the learning for the PN-unconserving $\mathbf{v}$ was similar to or even larger than that for the PN-conserving $\mathbf{v}$. The modeling of the BM that outputs zero precisely against several different inputs is seemingly a numerically diffcult task. In the PN approach, this requirement and related cost completely go away because the values of these PN-unconserving coefficients automatically vanish regardless of BM's parameters. This compactness in the PN approach indeed plays an advantageous role, as compared to the FS approach, in showing better performance even with $n_{\mathrm{reg}} = 6$. It should be strongly emphasized that the difficulties pointed out above in the FS treatment stem from the nature of our underlying ML model, as were also observed in the previous study based on the MCMC sampling, and are not fundamentally caused by our quantum algorithm of the state preparation.

Figure 3j to 3m show the errors of the PECs computed using the RBM model as a function of varying n_{h} with CMO and LMO basis in addition to testing $n_{\mathrm{reg}} = 8$ and 50. The results with $n_{\mathrm{reg}} = 50$ indicated that the RBM-based ANN state with $n_{\mathrm{h}} = 2$, the smallest RBM, is capable of reproducing the full CI energies across the curve with a near machine accuracy. The validity of our quantum algorithm for the preparation of the RBM state was confirmed even for enlarging n_{h}. Moreover, reducing n_{reg} to 8 for the state preparation for RBM still yields a reasonable accuracy in the energy prediction.

We attempted to closely analyze the effect of the roundoff errors in the energy register qubits on the coefficients $C_{\mathbf{v}}$.

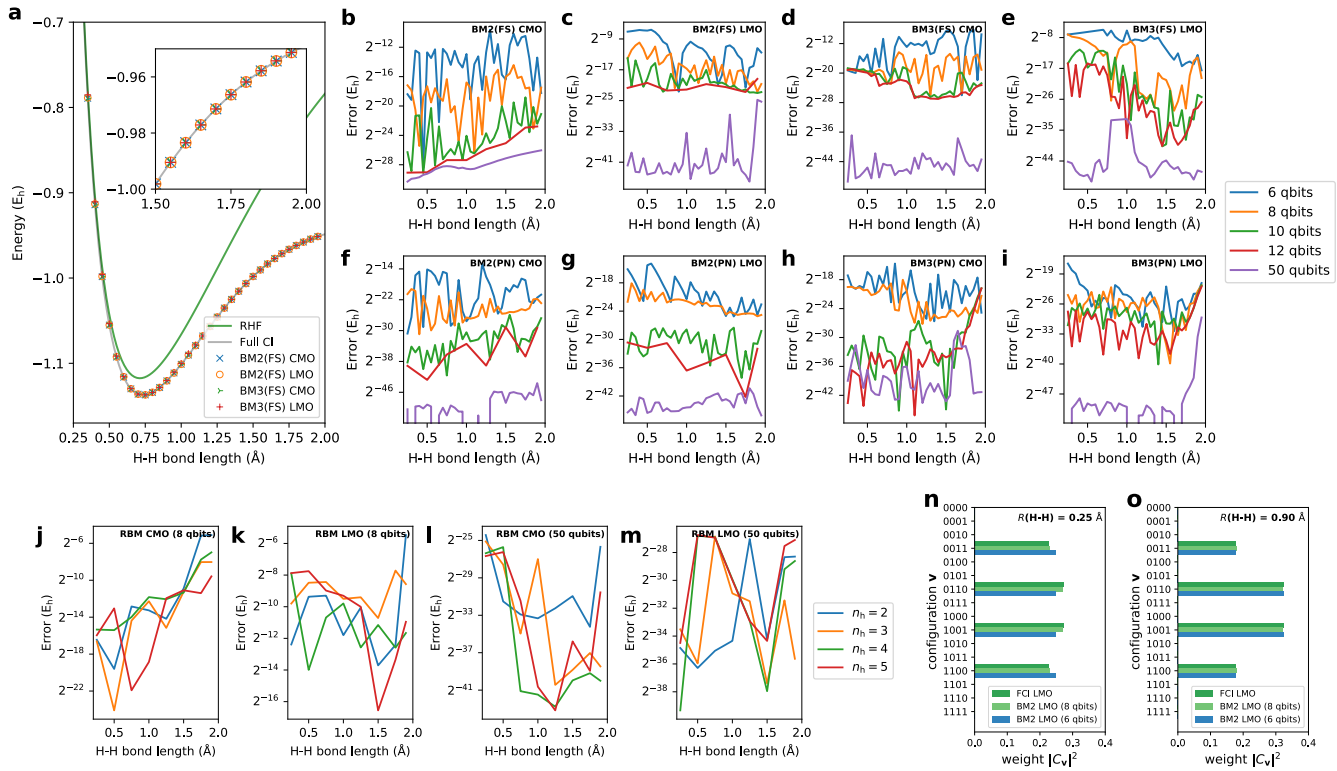

Figure 3: **a.** The bond dissociation energy curves of the H_2 molecule computed using BM2(FS) and BM3(FS) with CMO and LMO basis and n_{reg} = 8 along with RHF and full CI energies. The errors of the PECs relative to the full CI predictions for (**b**) BM2(FS)/CMO, (**c**) BM2(FS)/LMO, (**d**) BM3(FS)/CMO, (**e**) BM3(FS)/LMO, (**f**) BM2(PN)/CMO, (**g**) BM2(PN)/LMO, (**h**) BM3(PN)/CMO, and (**i**) BM3(PN)/LMO as a function of n_{reg} = 6, 8, 10, 12, and 50. The errors of the PECs obtained with RBM model with (**j**) CMO/n_{reg} = 8, (**k**) LMO/n_{reg} = 8, (**l**) CMO/n_{reg} = 50, and (**m**) LMO/n_{reg} = 50 as a function of n_{v} = 2, 3, 4, and 5. The distributions of the weights $|C_{\mathbf{v}}|^2$ determined by BM2/LMO with n_{reg} = 6 and 8 as well as full CI for bond lengths of (**n**) 0.25 and (**o**) 0.9 Å.

In Figure 3n to 3o, the distributions of the weights $|C_{\mathbf{v}}|^2$ determined by BM2/LMO with n_{reg} = 6 are shown for bond lengths of 0.25 and 0.9 Å. For comparison, the exact distributions taken from the corresponding full CI results are included in the graph. The errors in the BM distribution appear to be appreciable for the bond length of 0.25 Å, whereas they were negligible for 0.9 Å.

To scrutinize these errors, we here focus on the ratio of the weights between two configurations $\mathbf{v}$ and $\mathbf{v}'$. We found that the precision to represent the ratio $|C_{\mathbf{v}}|^2/|C_{\mathbf{v}'}|^2$ is in fact limited depending on n_{reg} and D, and formally written as $\exp(-2^{n_{\mathrm{reg}}} \cdot D)$. This limited precision stems from the finite binary representation of the energy register $\tilde{\mathbf{E}}_{\mathbf{v}}$ (eq. (9)). With the bond length of 0.25 Å, the exact ratio of the weights for $\mathbf{v}$ = (1100) and $\mathbf{v}'$ = (1001) is observed to be 1.20 (= 0.272/0.227) from the FCI result; however, the BM2 calculation with the resulting scaling constant D = 78 can express the ratio with a precision of 3.38 ($=\exp(-2^6 \cdot 78)$), which exceeds the exact one. This poor precision seems to underlie the errors in Figure 3n. On the other hand, the BM calculation with the bond length of 0.9 Å resulted in a scaling constant D = 38, and thus can express the ratio of the weights between $\mathbf{v}$ = (1100) and $\mathbf{v}'$ = (1001) with a precision of 1.81 ($= \exp(-2^6 \cdot 38)$). This precision is comparable to the ratio of the corresponding weight for full CI results, 1.83 (= 0.324/0.177); thus, the satisfactory accuracy in Figure 3o was delivered. The above discussion indicates that the scaling constant D plays a key role in determining the reliability but is an uncontrollable parameter. An increase in the number of the energy register qubits is a simple way to rectify the roundoff errors arising in $\mathbf{C}_{\mathbf{v}}$ and consequently enhance the accuracy of the energy prediction.

Relative Energies of *s-trans* and *s-cis* Butadiene

We next present the calculations of the relative energy of butadiene between the *s-trans* and *s-cis* isomers. Table 1 shows the total energies of *s-trans* and *s-cis* butadienes and the relative energies computed with BM2, BM3, and RBM models on a QC simulator along with the results at the RHF and CASCI levels of theory. The BM2 and BM3 models using LMO basis with n_{reg} = 8 yield the total and relative energies in good agreement with the CASCI results. The relative energies were predicted with an error of 0.01 $m\mathrm{E}_{\mathrm{h}}$, which is smaller than the error in the total energies, estimated to be 0.05 $m\mathrm{E}_{\mathrm{h}}$. The error cancellation in the relative energies is considered favorable in chemical applications. For the BM models using CMO basis, the errors in the total and relative energies were relatively large even with increasing n_{reg}. Figure S2 displays that the vanishing weights in the CASCI wavefunction are fewer with LMOs than with CMOs. As discussed earlier, this feature in the use of LMOs plays an advantageous role in the performance of the BM calculations.

As shown in Figure 4a, we monitored a training progress of the BM2/LMO energy for the *s-trans* isomer with various n_{reg}. The results with n_{reg} = 6 shows a largely oscillating behavior. This instability was relatively mitigated with

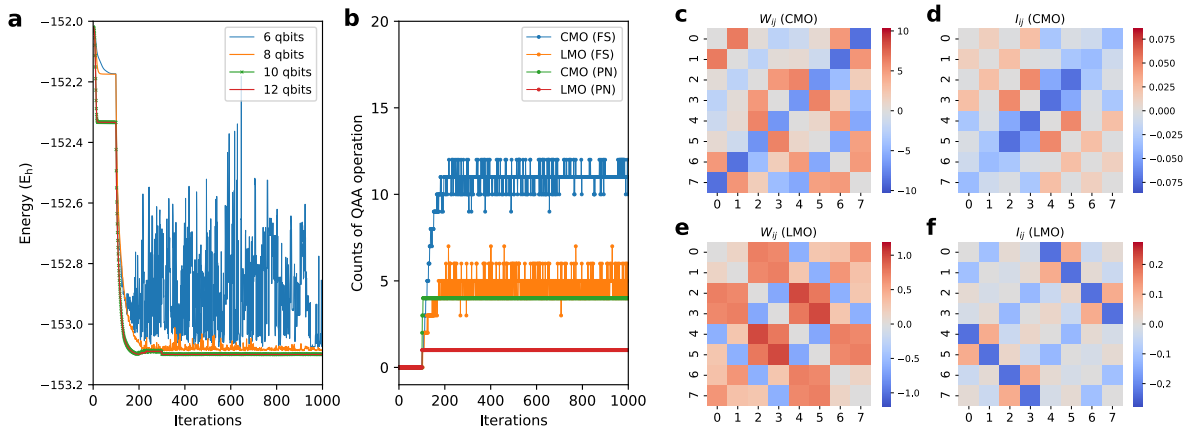

Figure 4: **a.** The progress of BM2/LMO energy as a function of training iteration for *s-trans* butadiene with n_{reg} = 6, 8, 10, and 12. **b.** The counts of QAA cycles as a progress of training of BM2 for CMO and LMO basis with FS and PN treatments. The heat maps of network parameters W_{ij} (eq. (17)) for (**c**) BM2/CMO and (**e**) BM2/LMO, and and of particle correlation I_{ij} (eq. (16)) for (**d**) BM2/CMO and (**f**) BM2/LMO, calculated for the *s-trans* isomer.

n_{reg} = 8. The ten or more energy register qubits were required to achieve stable training.

Figure 4b shows the number of QAA [38] cycles (Algorithm S4) to achieve a desired, amplified state in every state preparation process for the BM2 calculation of the *s-trans* isomer using n_{reg} = 8. The average number of the QAA operations per iteration varies depending on the orbital type (LMO or CMO) and on the particle-conservation treatment (PN or FS). Compared to the CMOs, the use of LMOs resulted in fewer QAA operations, which are a frequency of 1.0 and 4.5 times per iteration for the PN and FS treatment, respectively. This is related to the fact that when using the LMOs, the configuration distribution of the prepared state is widely spreading (see also Figure S2) to a more significant degree than the CMO case, and less dissimilar to that of the initial state that begins with a uniform distribution. The PN treatment plays a favorable role in reducing the cost associated with the amplification compared to the FN treatment. Note that marginalizing the hidden layer of RBM's $C_{\mathbf{v}}$ lowers the probability of the target state by a factor of approximately $\sqrt{2^{n}_{\mathrm{v}}}$; thus, the number of the QAA cycles required is much larger, scaling up exponentially with n_{v}, compared to the BM cases.

In Figure 4, we attempt to show a numerical comparison between the resulting ANN parameters and the physical quantities computed from the ANN state. Figure 4d and 4f are heat maps of the so-called particle correlation I_{ij}, [53]

$$I_{ij} \coloneqq \langle\Psi|\hat{n}_i\hat{n}_j|\Psi\rangle - \langle\Psi|\hat{n}_i|\Psi\rangle\langle\Psi|\hat{n}_j|\Psi\rangle \qquad (16)$$

evaluated with the trained BM2/CMO and BM2/LMO wavefunctions, respectively, for the *s-trans* isomer. The number operator $\hat{n}_i$ is written using the second-quantization operators as $\hat{n}_i = a_i^{\dagger}a_i$. We constructed a metric comparable to I_{ij} using a linear mixture of the ANN parameters a_i and w_{ij}. Although there is arbitrariness in the mixture, one given as

$$W_{ij} \coloneqq \left\{w_{ij} + (a_i + w_{ii})/6 + (a_j + w_{jj})/6\right\}(1 - \delta_{ij}) \qquad (17)$$

with the Kronecker delta δ_{ij} is shown in Figure 4c and e using the ANN parameters of the trained BM2/CMO and BM2/LMO models, respectively. Equation (17) is derived in terms of satisfying the relation $E^{\mathrm{BM2}}(\mathbf{v};\boldsymbol{\theta}) = \sum_{ij} v_i v_j W_{ij}$ for doubly-occupied $\mathbf{v}$. Interestingly, the heat maps of W_{ij} appear to capture some parts of the feature of those of the particle correlation I_{ij} for both LMO and CMO cases; however, there is no overall coherent relation between W_{ij} and I_{ij}.

Table 1: Predicted total energies (in $m\mathrm{E_h}$) of *s-trans* and *s-cis* butadiene and their energy difference ΔE (in $m\mathrm{E_h}$) using BM2, BM3 and RBM models using CMO and LMO basis with PN treatment. The total energies presented are subtracted from −153 $\mathrm{E_h}$.

	s-trans (CMO)	*s-cis* (CMO)	ΔE	*s-trans* (LMO)	*s-cis* (LMO)	ΔE
RHF	−16.49	−14.04	2.46			
CASCI	−102.70	−100.30	2.40	−102.70	−100.30	2.40
BM2						
6 qubits	−88.92	−85.00	3.92	−102.57	−100.11	2.46
8 qubits	−90.64	−85.88	4.77	−102.65	−100.25	2.41
50 qubits	−90.82	−86.09	4.73	−102.67	−100.26	2.41
BM3						
6 qubits	−88.05	−83.46	4.59	−102.55	−99.90	2.66
8 qubits	−9002	−87.03	3.00	−102.65	−100.27	2.38
50 qubits	−90.22	−87.24	2.98	−102.69	−100.30	2.39
RBM [a]						
8 qubits	−54.89	−52.69	2.20	−101.54	−99.20	2.35

[a] n_{v} = 4

PABI Potential Energy Curve Calculation

As a realistic test case, we here present the PEC calculation of the ring-opening isomerization reaction of the organic molecule, pentaarylbiimidazole (PABI) [54] (Figure 5a). This reaction, which is experimentally activated by photo-irradiation, affords a transient metastable species with the resonance hybrid of an open-shell biradical form and a closed-shell quinoid form of two dissociated imidazolyl moieties. Figure 5b shows the CMOs obtained from the RHF calculations and used as the active MOs in the CAS(4e,4o) treatment. The total energies of the S_0 state predicted with the BM models with LMO and CMO basis as a function of the progress of the ring-open reaction are displayed in Figure 5c. The BM models with six energy register qubits (n_{reg} = 6) were sufficiently accurate for capturing the formation of the high-energy meta-stable state at the open-ring structure, which was confirmed in the previous spectroscopic research. [54] The errors of the PECs relative to the CAS-CI results indicate that the energies of BM2 with n_{reg} = 6 are

accurate to an error of less than 1 $m\mathrm{E_h}$. An increase in n_{reg} and the connectivity order of the BM is apt to improve the accuracy that approaches the CAS-CI quality (Figure 5d and e).

Figure 5f and 5g show the natural orbital occupation numbers (NOONs) of the state calculated at the closed-ring and open-ring geometries, respectively. This analysis shows that the electronic character of the closed-ring structure is of the quinoidal nature, which is within the single-determinant picture using CMO basis, whereas the open-shell biradical nature emerges at the open-ring structure as is reflected by the half-integer NOONs of NO2 and NO3, which are approximately 1.6 and 0.4, respectively. As indicated by the distribution of the configurations (Figure S4), the biradical state is of multireference (or strongly-corrected) electronic character. These calculations thus demonstrated that our quantum computation of the BM-based models is within reach of accurate multireference wavefunction calculations that involve a variation between quinoidal and radical nature.

3 Conclusions

In this work, a formalism based on the use of quantum gates to form the ML-inspired quantum state, NQS, with the BM2, BM3, and RBM energy functions on a QC has been developed for the materialization of neural networks trained as quantum chemical objects. Qubits play a role in quantum-mechanically representing bitstrings of occupancies of configurations, which are descriptors of this ANN model. With the energy and its gradients estimated via quantum measurements, the training of the network parameters towards learning the superposition structure of the CAS-CI state is efficiently performed by classical computations. The marked features of the present NQS preparation algorithm are as follows:

1. The process to prepare the HBM-based NQS representing the CAS-CI state is fully quantum-native, forgoing the random sampling of the intermediate state done in the approach by Xia and Kais.
2. Kitaev's QPE[36,37] is exploited to evaluate the BM energy functions via its phase kickback trick with a flavor similar to the GEQS algorithm[28] of the general-purpose QML. Unlike the way of using the QPE in Hamiltonian evolution as done by Aspuru-Guzik *et al.* and others,[45,55–57] our approach for preparing a single NQS uses it in a noniterative manner with no time evolution nor Trotter steps.
3. The rescaling parameters for the energy function have to be determined, requiring an additional quantum treatment subject to the QUBO problem[50] to find the maximum and minimum of a function.
4. The values of the rescaled energy functions with a bit-vector representation are efficiently calculated and stored into a given number of energy register qubits, which can thus suffer the roundoff errors. In our test cases, the use of ten energy register qubits showed satisfactorily convergent results.
5. The key factor determining the depth of NQS's quantum circuits is the number of the QAA cycles to amplify the probability of the desired state. We found that it can be relatively small if the resultant state is near maximally entangled or highly multireference.
6. The NQS described in this study is a hybrid quantum-classical algorithm and classified as a VQE type.
7. The HBM energy functions with no hidden nodes, namely BM2, BM3, or even higher-order, are a suited class of underlying ANNs for NQS prepared on a QC. With HBM, our approach allows for the estimation of *analytical* gradients of the energy with respect to network parameters using the prepared NQS state, just as the energy is calculated from the expectation values of Pauli strings.
8. As analyzed in Section S1.7, the number of QAA cycles (N_{QAA}) is a critical factor in determining the depth of the quantum circuits in NQS. N_{QAA} varies depending on systems and basis types, and is apt to be small in multireference cases.
9. Formulation with the RBM model for our quantum algorithm is straightforward; however, several concerns are aroused in the implementation. (i) the gradients of the energy cannot be analytically computed on a QC as a sum of the expectation values of Pauli strings because of the involvement of the sigmoid function, which is in contrast absent in HBM. (ii) With an increasing number of the hidden nodes, the qubits proportionally increase in number. Contrarily, HBM has no dependence of the number of qubits on its order. (iii) Our testing on the simulator revealed that marginalizing the hidden layer of RBM's $C_{\mathbf{v}}$ lessens the probability of the target state by a factor of approximately $\sqrt{2^{n_{\mathrm{v}}}}$ in Gibbs state preparation. This means that N_{QAA} grows rapidly with increasing n_{v}.

We have confirmed on the simulator that the quantum algorithm (Algorithm 1) is implementable with the use of elementary quantum gates except for the process to determine D and Δ, and formally involves no approximation to the given NQS ansatz except the roundoff errors due to the finite precision of the energy register. The NQS calculations simulated for illustrative molecules overall reproduced the ground-state CAS-CI energy and wavefunction with high accuracy when the computational conditions were properly given. The errors of the trained NQS compared to the CAS-CI wavefunction are fundamentally irrelevant to the use of quantum state preparation proposed in this work, and are the same nature of error as what was observed in the fully classical NQS scheme studied in the previous work. The fully visible nature of the HBM neural networks plays a crucial role in its good accommodation to a quantum algorithm, and this special usability of HBM introduced in our previous study for NQS should benefit the general-purpose QML.

4 Methods

Our hybrid quantum-classical algorithm for determining the NQS was implemented into a Python-based computer code fully running on a conventional computer as a prototype (see also Section S1.8 for details). We performed benchmark calculations on three molecular systems; the hydrogen molecule H_2, butadiene C_4H_6, and pentaarylbiimidazole (PABI)[54] $C_{36}H_{24}N_4$. The STO-3G basis set[58] was throughout used for the atomic orbital basis to represent the second-quantized form of Hamiltonian. The canonical molecular orbitals (CMOs) were determined at the restricted Hartree-Fock (RHF) level of theory. For H_2, HOMO and LUMO were used as the molecular orbitals considered in

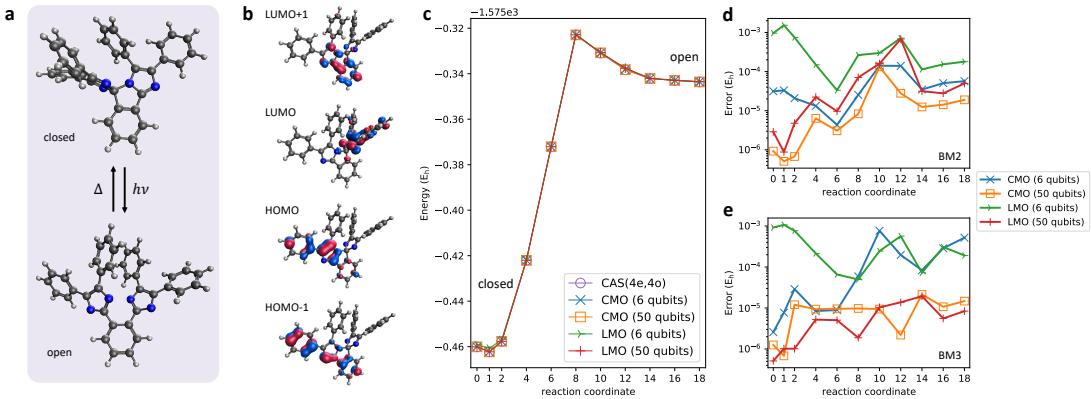

f Natural orbital occupation numbers of closed-ring structure (coordination #1)

	NO1	NO2	NO3	NO4
BM2 8 qubits	2.00	2.00	0.00	0.00
BM2 50 qubits	2.00	1.99	0.01	0.00
CASCI	2.00	1.99	0.01	0.00

g Natural orbital occupation numbers of open-ring structure (coordination #18)

	NO1	NO2	NO3	NO4
BM2 8 qubits	2.00	1.61	0.39	0.00
BM2 50 qubits	2.00	1.59	0.41	0.00
CASCI	2.00	1.59	0.41	0.00

Figure 5: **a.** Molecular structures of closed-ring and open-ring form of pentaarylbiimidazole (PABI). **b.** Active orbitals considered in the CAS-CI(4e,4o) treatment. **c.** Potential energies curves of the ring-opening isomerization reaction of PABI calculated with full CI and with the BM2 model using CMO and LMO basis with n_{reg} = 6 and 50. The errors of PEC energies predicted with (**d**) BM2 and (**e**) BM3 relative to the full CI values. The NOONs of the ground state calculated at the (**f**) closed-ring and (**g**) open-ring geometries.

the calculation, referred to as active orbitals. For butadiene and PABI, HOMO-1, HOMO, LUMO, and LUMO+1 were used as the active orbitals. With these orbital setups, our quantum chemical models of the systems correspond to the complete-active-space (CAS) treatment[24,25] with two electrons in two orbitals, denoted CAS(2e,2o), for H_2, and CAS(4e,4o) for butadiene and PABI. The localized molecular orbitals (LMOs) were additionally obtained by the unitary transformation of the active orbitals via the Pipek-Mezey localization scheme.[59] Two kinds of the active-space Hamiltonian for a given system were constructed with CMOs and LMOs, respectively, and used for NQS calculations as different test cases. The entanglement structures of the resultant NQS wavefunctions should differ depending on the orbital types. This nature was exploited in order to assess our approaches against different entanglement characters with the same system.

The bond dissociation energy curves of H_2 were calculated with the bond length ranging from 0.25 to 1.95 Å. The geometries of cis- and trans-conformers of 1,3-butadiene, which were determined by the geometry optimization at B3LYP/cc-pVDZ level of theory,[60,61] are provided in Supporting Information. All the single-point structures used in the potential energy curve (PEC) calculations for the electrocyclic reaction of the PABI are tabulated in Supporting Information.

Two types of the initial state for the visible qubits in the state preparation of NQS were used. They change the treatment of the particle-number subspaces. The first type is the Hadamard-transformed state, as written in Section 2, involving $2^{n_{\mathrm{v}}}$ basis states, which are complete with spanning the Fock space for the given second-quantized Hamiltonian. The use of this initial state, designated FS, considers all possible numbers of electrons with arbitrary spins in constructing NQS. The second type is the particle-number (PN) state, prepared using the quantum circuit shown by Gard et al.[51] It is an equally-weighted superposition like the Hadamard-transformed state but only using the basis states with a desired number of electrons. The PN-conserving initial state undergoes our state preparation process, resulting in the formation of an NQS as a superposition of these PN conserving basis states. Figure S1 shows a PN circut used as the initial state for the CAS(4e,4o) calculations. The BM2 and BM3 states prepared with the FS treatment are denoted BM2(FS) and BM3(FS), respectively, while those with the PN-conserving basis states were denoted BM2(PN) and BM3(PN), respectively.

The trained NQS models with BM2 and BM3 were obtained for all the systems. We tested the various number of the energy register qubits to gauge its impact on the accuracy in the prepared state. The examined n_{reg} was 6, 8, 10, and 12 for H_2 and C_4H_6, and 6 for PABI. For comparison, the reference data were obtained with 50 energy register qubits, offering near double-precision accuracy. The RBM energies were calculated for H_2 with n_{reg} set to 8 and 50 and for butadiene with n_{reg} set to 8. The numbers of hidden nodes (n_{h}) were tested to be 2, 3, 4, and 5 for H2 and 4 for butadiene. As shown in Figure 4a, with n_{reg} = 6, where obtaining stable convergence was difficult, we used the lowest of the energies of the training history as the energy of the solution.

It should be noted that the noise and system errors were not considered in all the quantum-computing simulations.

Acknowledgment

M.H. thanks Hattori International Scholarship Foundation for support. T.Y. is supported by JSPS KAKENHI (Grant No. 21H01881, 21K18931, and JPJSBP120229601) and JST PRESTO (Grant No. 17937609). M.S. is supported by JST FOREST Program, Grant Number JPMJFR206J.

References

(1) E., H. G.; R., S. R. Reducing the Dimensionality of Data with Neural Networks. *Science* **2006**, *313*, 504–507.

(2) Jumper, J. et al. Highly accurate protein structure prediction with AlphaFold. *Nature* **2021**, *596*, 583–589.

(3) James, K. et al. Pushing the frontiers of density functionals by solving the fractional electron problem. *Science* **2021**, *374*, 1385–1389.

(4) Duvenaud, D. K.; Maclaurin, D.; Iparraguirre, J.; Bombarell, R.; Hirzel, T.; Aspuru-Guzik, A.; Adams, R. P. Convolutional Networks on Graphs for Learning Molecular Fingerprints. Advances in Neural Information Processing Systems. 2015.

(5) Smith, J. S.; Isayev, O.; Roitberg, A. E. ANI-1: an extensible neural network potential with DFT accuracy at force field computational cost. *Chemical Science* **2017**, *8*, 3192–3203.

(6) Schütt, K. T.; Chmiela, S.; von Lilienfeld, O. A.; Tkatchenko, A.; Tsuda, K.; Müller, K.-R. Machine Learning Meets Quantum Physics. *Lecture Notes in Physics* **2020**,

(7) Carleo, G.; Troyer, M. Solving the Quantum Many-Body Problem with Artificial Neural Networks. *Science* **2017**, *355*, 602–606.

(8) Torlai, G.; Mazzola, G.; Carrasquilla, J.; Troyer, M.; Melko, R.; Carleo, G. Many-body quantum state tomography with neural networks. *Nat. Phys.* **2018**, *14*, 447–450.

(9) Carleo, G.; Nomura, Y.; Imada, M. Constructing exact representations of quantum many-body systems with deep neural networks. *Nat. Commun.* **2018**, *9*, 5322.

(10) Melko, R. G.; Carleo, G.; Carrasquilla, J.; Cirac, J. I. Restricted Boltzmann machines in quantum physics. *Nat. Phys.* **2019**, *15*, 887–892.

(11) Choo, K.; Mezzacapo, A.; Carleo, G. Fermionic neural-network states for ab-initio electronic structure. *Nat. Commun.* **2020**, *11*, 2368.

(12) Sharir, O.; Levine, Y.; Wies, N.; Carleo, G.; Shashua, A. Deep Autoregressive Models for the Efficient Variational Simulation of Many-Body Quantum Systems. *Phys. Rev. Lett.* **2020**, *124*, 020503.

(13) Torlai, G.; Melko, R. G. Machine-Learning Quantum States in the NISQ Era. *Annu. Rev. Condens. Matter Phys.* **2020**, *11*, 325–344.

(14) Xia, R.; Kais, S. Quantum machine learning for electronic structure calculations. *Nat. Commun.* **2018**, *9*, 4195.

(15) Yang, P.-J.; Sugiyama, M.; Tsuda, K.; Yanai, T. Artificial Neural Networks Applied as Molecular Wave Function Solvers. *J. Chem. Theory Comput.* **2020**, *16*, 3513–3529.

(16) Pfau, D.; Spencer, J. S.; Matthews, A. G. D. G.; Foulkes, W. M. C. Ab initio solution of the many-electron Schrödinger equation with deep neural networks. *Phys. Rev. Res.* **2020**, *2*, 033429.

(17) Hermann, J.; Schätzle, Z.; Noé, F. Deep-neural-network solution of the electronic Schrödinger equation. *Nat. Chem.* **2020**, *12*, 891–897.

(18) Spencer, J. S.; Pfau, D.; Botev, A.; Foulkes, W. M. C. Better, faster fermionic neural networks. *arXiv preprint arXiv:2011.07125* **2020**,

(19) Barrett, T. D.; Malyshev, A.; Lvovsky, A. I. Autoregressive neural-network wavefunctions for ab initio quantum chemistry. *Nat. Mach. Intell.* **2022**, *4*, 351–358.

(20) Yoshioka, N.; Mizukami, W.; Nori, F. Solving quasiparticle band spectra of real solids using neural-network quantum states. *Commun. Phys.* **2021**, *4*, 106.

(21) Hsieh, C. Y.; Sun, Q.; Zhang, S.; Lee, C. K. Unitary-coupled restricted Boltzmann machine ansatz for quantum simulations. *npj Quantum Information* **2021**, *7*, 19.

(22) Kanno, S.; Tada, T. Many-body calculations for periodic materials via restricted Boltzmann machine-based VQE. *Quantum Sci. Technol.* **2021**, *6*, 025015.

(23) Sureshbabu, S. H.; Sajjan, M.; Oh, S.; Kais, S. Implementation of Quantum Machine Learning for Electronic Structure Calculations of Periodic Systems on Quantum Computing Devices. *Journal of Chemical Information and Modeling* **2021**, *61*, 2667–2674.

(24) Roos, B. O.; Taylor, P. R.; Sigbahn, P. E. M. A complete active space SCF method (CASSCF) using a density matrix formulated super-CI approach. *Chem. Phys.* **1980**, *48*, 157–173.

(25) Roos, B. O.; Lindh, R.; Malmqvist, P. A.; Veryazov, V.; Widmark, P.-O. *Multiconfigurational Quantum Chemistry*, 1st ed.; John Wiley and Sons, Inc.: New Jersey, 2016.

(26) Luo, S.; Sugiyama, M. Bias-variance trade-off in hierarchical probabilistic models using higher-order feature interactions. Proceedings of the AAAI Conference on Artificial Intelligence. 2019; pp 4488–4495.

(27) Sejnowski, T. J. Higher-order Boltzmann machines. *AIP Conf. Proc.* **1986**, *151*, 398–403.

(28) Wiebe, N.; Kapoor, A.; Svore, K. M. Quantum Deep Learning. *Quantum Info. Comput.* **2016**, *16*, 541–587.

(29) Giovannetti, V.; Lloyd, S.; Maccone, L. Quantum Random Access Memory. *Phys. Rev. Lett.* **2008**, *100*, 160501.

(30) Poulin, D.; Wocjan, P. Sampling from the Thermal Quantum Gibbs State and Evaluating Partition Functions with a Quantum Computer. *Phys. Rev. Lett.* **2009**, *103*, 220502.

(31) Biamonte, J.; Wittek, P.; Pancotti, N.; Rebentrost, P.; Wiebe, N.; Lloyd, S. Quantum machine learning. *Nature* **2017**, *549*, 195–202.

(32) Mitarai, K.; Negoro, M.; Kitagawa, M.; Fujii, K. Quantum circuit learning. *Phys. Rev. A* **2018**, *98*, 032309.

(33) Cong, I.; Choi, S.; Lukin, M. D. Quantum convolutional neural networks. *Nat. Phys.* **2019**, *15*, 1273–1278.

(34) Havlíček, V.; Córcoles, A. D.; Temme, K.; Harrow, A. W.; Kandala, A.; Chow, J. M.; Gambetta, J. M. Supervised learning with quantum-enhanced feature spaces. *Nature* **2019**, *567*, 209–212.

(35) García, D. P.; Cruz-Benito, J.; García-Peñalvo, F. J. Systematic Literature Review: Quantum Machine Learning and its applications. *arXiv preprint arXiv:2201.04093* **2022**,

(36) Kitaev, A. Y. Quantum measurements and the Abelian stabilizer problem. *arXiv preprint quant-ph/9511026* **1995**,

(37) Cleve, R.; Ekert, A.; Macchiavello, C.; Mosca, M. Quantum algorithms revisited. *Proc. R. Soc. A: Math. Phys. Eng. Sci.* **1998**, *454*, 339–354.

(38) Brassard, G.; Hoyer, P.; Mosca, M.; Tapp, A. Quantum amplitude amplification and estimation. *Contemporary Mathematics* **2002**, *305*, 53–74.

(39) Cao, Y.; Romero, J.; Olson, J. P.; Degroote, M.; Johnson, P. D.; Kieferová, M.; Kivlichan, I. D.; Menke, T.; Peropadre, B.; Sawaya, N. P. D.; Sim, S.; Veis, L.; Aspuru-Guzik, A. Quantum Chemistry in the Age of Quantum Computing. *Chem. Rev.* **2019**, *119*, 10856–10915.

(40) McArdle, S.; Endo, S.; Aspuru-Guzik, A.; Benjamin, S. C.; Yuan, X. Quantum computational chemistry. *Rev. Mod. Phys.* **2020**, *92*, 015003.

(41) Bauer, B.; Bravyi, S.; Motta, M.; Chan, G. K.-L. Quantum Algorithms for Quantum Chemistry and Quantum Materials Science. *Chem. Rev.* **2020**, *120*, 12685–12717.

(42) Bharti, K.; Cervera-Lierta, A.; Kyaw, T. H.; Haug, T.; Alperin-Lea, S.; Anand, A.; Degroote, M.; Heimonen, H.; Kottmann, J. S.; Menke, T.; Mok, W.-K.; Sim, S.; Kwek, L.-C.; Aspuru-Guzik, A. Noisy intermediate-scale quantum algorithms. *Rev. Mod. Phys.* **2022**, *94*, 015004.

(43) Tilly, J.; Chen, H.; Cao, S.; Picozzi, D.; Setia, K.; Li, Y.; Grant, E.; Wossnig, L.; Rungger, I.; Booth, G. H., et al. The Variational Quantum Eigensolver: a review of methods and best practices. *arXiv preprint arXiv:2111.05176* **2021**,

(44) Anand, A.; Schleich, P.; Alperin-Lea, S.; Jensen, P. W. K.; Sim, S.; Díaz-Tinoco, M.; Kottmann, J. S.; Degroote, M.; Izmaylov, A. F.; Aspuru-Guzik, A. A quantum computing view on unitary coupled cluster theory. *Chem. Soc. Rev.* **2022**, *51*, 1659–1684.

(45) Alán, A.-G.; D., D. A.; J., L. P.; Martin, H.-G. Simulated Quantum Computation of Molecular Energies. *Science* **2005**, *309*, 1704–1707.

(46) Peruzzo, A.; McClean, J.; Shadbolt, P.; Yung, M.-H.; Zhou, X.-Q.; Love, P. J.; Aspuru-Guzik, A.; O'Brien, J. L. A variational eigenvalue solver on a photonic quantum processor. *Nat. Commun.* **2014**, *5*, 4213.

(47) Grimsley, H. R.; Economou, S. E.; Barnes, E.; Mayhall, N. J. An adaptive variational algorithm for exact molecular simulations on a quantum computer. *Nat. Commun.* **2019**, *10*, 3007.

(48) Huggins, W. J.; O'Gorman, B. A.; Rubin, N. C.; Reichman, D. R.; Babbush, R.; Lee, J. Unbiasing fermionic quantum Monte Carlo with a quantum computer. *Nature* **2022**, *603*, 416–420.

(49) Torlai, G.; Mazzola, G.; Carleo, G.; Mezzacapo, A. Precise measurement of quantum observables with neural-network estimators. *Phys. Rev. Res.* **2020**, *2*, 022060.

(50) Pastorello, D.; Blanzieri, E. Quantum annealing learning search for solving QUBO problems. *Quantum Inf. Process.* **2019**, *18*, 1–17.

(51) Gard, B. T.; Zhu, L.; Barron, G. S.; Mayhall, N. J.; Economou, S. E.; Barnes, E. Efficient symmetry-preserving state preparation circuits for the variational quantum eigensolver algorithm. *npj Quantum Inf.* **2020**, *6*, 1–9.

(52) Suzuki, Y. et al. Qulacs: a fast and versatile quantum circuit simulator for research purpose. *Quantum* **2021**, *5*, 559.

(53) Hachmann, J.; Dorando, J. J.; Avilés, M.; Chan, G. K.-L. The

radical character of the acenes: A density matrix renormalization group study. *J. Chem. Phys.* **2007**, *127*, 134309.

(54) Kobayashi, Y.; Okajima, H.; Sotome, H.; Yanai, T.; Mutoh, K.; Yoneda, Y.; Shigeta, Y.; Sakamoto, A.; Miyasaka, H.; Abe, J. Direct Observation of the Ultrafast Evolution of Open-Shell Biradical in Photochromic Radical Dimer. *J. Am. Chem. Soc.* **2017**, *139*, 6382–6389.

(55) Dobšíček, M.; Johansson, G.; Shumeiko, V.; Wendin, G. Arbitrary accuracy iterative quantum phase estimation algorithm using a single ancillary qubit: A two-qubit benchmark. *Phys. Rev. A* **2007**, *76*, 03030.

(56) Seth, L. Universal Quantum Simulators. *Science* **1996**, *273*, 1073–1078.

(57) Abrams, D. S.; Lloyd, S. Simulation of Many-Body Fermi Systems on a Universal Quantum Computer. *Phys. Rev. Lett.* **1997**, *79*, 2586–2589.

(58) Hehre, W. J.; Stewart, R. F.; Pople, J. A. Self-Consistent Molecular-Orbital Methods. I. Use of Gaussian Expansions of Slater-Type Atomic Orbitals. *J. Chem. Phys.* **1969**, *51*, 2657–2664.

(59) Pipek, J.; Mezey, P. G. A fast intrinsic localization procedure applicable for ab initio and semiempirical linear combination of atomic orbital wave functions. *J. Chem. Phys.* **1989**, *90*, 4916–4926.

(60) Becke, A. D. Density-functional thermochemistry. III. The role of exact exchange. *J. Chem. Phys.* **1993**, *98*, 5648–5652.

(61) Dunning, T. H. Gaussian basis sets for use in correlated molecular calculations. I. The atoms boron through neon and hydrogen. *J. Chem. Phys.* **1989**, *90*, 1007–1023.